

Metal–Organic Framework Separator as a Polyselenide Filter for High-Performance Lithium–Selenium Batteries

Md. Anwar Hossain, Sarttrawut Tulaphol, Arjun K. Thapa, Mohammad Shahinur Rahaman, Jacek B. Jasinski, Hui Wang, Mahendra K. Sunkara, Jaroslaw Syzdek, Osman K. Ozdemir, Jason M. Ornstein, and Noppadon Sathitsuksanoh*



Cite This: <https://doi.org/10.1021/acsaem.1c01806>



Read Online

ACCESS |



Metrics & More



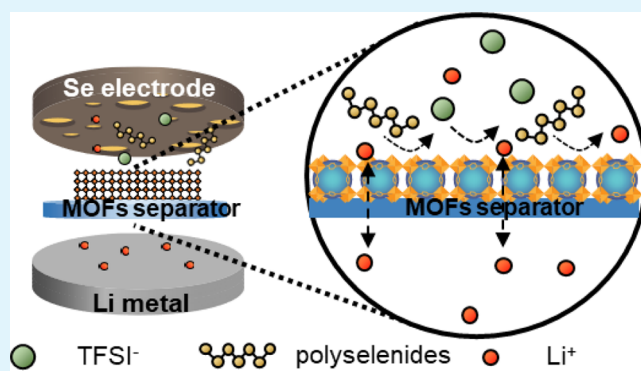
Article Recommendations



Supporting Information

ABSTRACT: Rapid self-discharge, poor cycling stability, and low Coulombic efficiency from polyselenide shuttling have retarded practical applications of lithium–selenium batteries. Here, we show that a cation-selective PCN separator of PCN-250(Fe) metal–organic frameworks coated on a porous polypropylene membrane suppresses polyselenide shuttle and enhances lithium-ion transport in lithium–selenium batteries. The Lewis acid sites of this PCN separator acted as selective barriers that immobilized polyselenides and provided uniform and stable lithium nucleation and growth during cycling. Lithium–selenium cells with the PCN separator had a stable and reversible electrochemical performance with a high discharge capacity of 423 mAh/g at C/5 and a Coulombic efficiency of >98% for 500 cycles. This work provides a guide for developing high-performance lithium–selenium batteries by a cation-selective separator strategy. This PCN separator can be applied to alkali-metal and alkali-metal chalcogenide battery systems.

KEYWORDS: metal–organic frameworks, polyselenides, shuttle effect, TFSI anions, lithium–selenium, batteries



1. INTRODUCTION

The great demand for electric vehicles and power-grid energy storage has stimulated the search for high-capacity rechargeable batteries. For decades, conventional lithium-ion batteries have been used for electronic devices. However, current transition metal oxide cathodes¹ have a low theoretical energy density (~ 350 to 450 mAh/g),² which prevents their practical application such as in electric vehicles.³ Thus, chalcogenide-containing cathodes, such as S, Se, and Te, have gained attention.^{4–7} Selenium is viewed as a potential electrode material in lithium–selenium cells because selenium has a high theoretical capacity (678 mAh/g)⁸ and a volumetric capacity comparable to lithium–sulfur batteries (3268 mAh/cm³ for selenium and 3467 mAh/cm³ for sulfur).^{9–12} Moreover, selenium has a high electrical conductivity of 1×10^{-3} S/cm,^{13–15} compared with sulfur (5×10^{-28} S/cm);¹⁶ the high conductivity provides selenium with better electrochemical properties. However, the performance of lithium–selenium batteries is impaired by the shuttling of soluble polyselenide (Se_x^{2-} , $4 \leq x \leq 8$)^{14,17} across a separator; the polyselenides react with the lithium metal electrode, which causes capacity fade. Moreover, uncontrolled diffusion of electrolyte anions, typically bis(trifluoromethanesulfonyl)imide (TFSI[−]), causes a nonuniform Li⁺ deposition on the Li anode and promotes Li dendrite formation. These issues hinder the development and

practical use of lithium–selenium batteries. The ability to prevent the shuttle effect of polyselenides and diffusion of anions will boost the electrochemical performance and life of lithium–selenium cells.

The separator provides the path for transporting cations, anions, and an electrolyte between electrodes. Porous polypropylene has been used widely as a separator, a key component of lithium–selenium cells. However, the weak interaction between carbon–carbon backbones of the polypropylene separator with polyselenides and TFSI anions results in the diffusion of polyselenides between electrodes, active material loss, self-discharge, and capacity fade.^{18–21} Modifying the separator to prevent polyselenides and anion diffusion is expected to tackle this problem.

Metal–organic frameworks (MOFs) are a class of porous solids with uniform pore structures and coordinated unsaturated sites. MOFs have narrow pore widths and

Received: June 23, 2021

Accepted: November 4, 2021

interconnected pores that enable the diffusion of Li^+ and function as a physical barrier to larger ions in an electrolyte. Moreover, MOFs have coordinated unsaturated sites (Lewis acid characteristics) that can capture Lewis bases, such as polyselenides²² and TFSI anions.²³ Among various MOFs, PCN-250²⁴ (also known as MIL-127 and Fe-soc-MOF²⁵) is a class of MOFs constructed from trinuclear iron oxo clusters ($\text{Fe}_3\text{-}\mu^3\text{-oxo}$ clusters) and tetratopic azobenzene-based linkers (3,3',5,5'-azobenzene tetracarboxylate) (Figure S1).²⁶ PCN-250 has a small pore width of 5.9 Å²⁷ and a high surface area of $\sim 1500 \text{ m}^2/\text{g}$. This MOF is robust and stable in solutions with pH 1 to 12.^{28,29} These characteristics make PCN-250 a good candidate as a separator modifier.

Here, we fabricated a modified separator using PCN-250 and assessed its ability to suppress the diffusion of polyselenides and TFSI anions in lithium–selenium batteries. We constructed the Se cathode by encapsulating the Se in activated carbon. We chose this cathode system because it has visible selenium cathode dissolution,³⁰ which enabled our study on the interaction of the PCN separator with polyselenides. We found that the PCN-modified separator inhibited the diffusion of polyselenides and TFSI anions from the cathode to the anode. As a result, the lithium–selenium cells were cycled at C/5 and 1C for 500 cycles with high-capacity retention.

2. EXPERIMENTAL SECTION

2.1. Materials. All reagents were used as received. Their manufacturers, purity, and CAS numbers are shown in Table S1. PCN-250 metal–organic frameworks (MOFs) were provided by Framergy, Inc. (College Station, TX) and produced under the commercial name AYRSORB F250. The physicochemical properties of PCN-250 are shown in Figure S2 (see the Supporting Information for details).

2.2. Synthesis of Selenium Encapsulated Activated Carbon Cathode (Se@AC). Selenium was loaded into activated carbon by a facial melt diffusion method to form Se@AC.³¹ In short, dry activated carbon and selenium in a 2:3 ratio by weight were ball milled at 300 rpm in acetone for 1 h. After ball milling, the selenium and activated carbon mixture was dried at 80 °C for 6 h to remove the acetone. The dry selenium-activated carbon mixture was heated under N_2 at 10 °C/min and held isothermally at 260 °C for 20 h. Finally, the sample was heated to 350 °C for 3 h to remove physisorbed selenium and cooled to ambient temperature. The selenium loading in Se@AC was $\sim 47 \text{ wt } \%$, measured by thermogravimetric analysis (Figure S3).

2.3. Characterization of Metal–Organic Frameworks. Powder X-ray diffraction (pXRD) analysis of MOF samples was performed on a Bruker D8 Discover diffractometer (Billerica, MA) using Cu $K\alpha$ radiation in the 2θ range from 10 to 40° with 0.5 s/step. N_2 adsorption/desorption was measured with a Micromeritics Tristar (Norcross, GA) instrument to calculate the MOF surface area and pore volume. Before the measurement, the sample was treated at 150 °C for 4 h with a Micromeritics FlowPrep with a sample degasser (Norcross, GA). The surface area, S_{BET} , was determined from N_2 isotherms using the Brunauer–Emmett–Teller equation (BET) based on the MOF overall mass. The pore size distribution of the PCN-250 MOF was calculated from the desorption isotherm using the nonlocal density functional theory (NLDFIT) model. The morphology and elemental mapping analyses of the interface between the PCN-250 layer and polypropylene were investigated using a scanning electron microscope (Tescan Vega V3, SEM) with an energy-dispersive X-ray spectrometry (EDS) analyzer.

Infrared spectra of the PCN-250 MOFs were recorded on a JASCO Fourier transform infrared (FTIR) spectrometer (Easton, MD), equipped with an attenuated total reflection stage (ATR). Samples were scanned in the spectral range between 400 and 4000 cm^{-1} at a 4 cm^{-1} resolution. Diffuse reflectance infrared Fourier transform

spectroscopy (DRIFTS) with adsorbed pyridine was performed to characterize acid sites; measurements were made with a JASCO FTIR equipped with a high-temperature DiffuseIR cell (PIKE Technology, WI). We chose pyridine as an *in situ* titrant for probing the Lewis acid site density of MOFs because of earlier success in observation of Lewis acid sites in other MOFs.^{32–34} The protocol for the DRIFTS experiments with temperature program desorption is described elsewhere with a slight modification.^{35,36} In short, MOF samples ($\sim 5 \text{ mg}$) were placed in a cylindrical alumina crucible and treated in nitrogen gas (50 mL/min) at 50–250 °C for 30 min unless otherwise noted. After the treatment, the DRIFTS spectra of MOF catalysts were recorded as the background spectra. The MOF materials were then saturated with pyridine vapor. The adsorbed pyridine was removed by flushing with N_2 gas at 50, 100, 150, or 250 °C for 30 min before recording the DRIFTS spectra. All spectra were recorded with 256 scans between 4000 and 400 cm^{-1} at a 4 cm^{-1} resolution.

XPS spectra were measured using a VG Scientific MultiLab 3000 ultrahigh vacuum surface analysis system, equipped with a dual-anode Mg/Al X-ray source and a CLAM4 hemispherical electron energy analyzer. The measurements were performed at the base pressure of 10^{-9} Torr range using non-monochromatized Al $K\alpha$ X-ray radiation ($h\nu = 1486.6 \text{ eV}$). The C–C peak of adventitious carbon at 284.8 eV was used for the binding energy (BE) calibration.

2.4. Fabrication of PCN-250 Coated Separators. Throughout this manuscript, we refer to the PCN-250-coated separator as a PCN separator. The PCN-250 particles (average particle size of 10 μm with SEM imagery; see the Supporting Information, Figure S4) were dried at 150 °C under a 70 cc/min N_2 flow overnight to remove moisture before using. PCN separators were fabricated by layering PCN-250 and the PVDF-HFP binder. In short, $\sim 0.03 \text{ g}$ of dry PCN-250 (0.1 wt %) was dispersed in ethanol and sonicated for 1 hour to disperse PCN. The PCN solution (10 mL) was filtered through a conventional polypropylene 2400 membrane. Next, the pump was turned off to allow the PCN to distribute on the polypropylene membrane. Then, 0.5 mL of PVDF-HFP in acetone (5 wt %) was filtered on top of the PCN layer to bind the PCN particles. The PCN and PVDF-HFP solutions were filtered alternately three times to ensure an even distribution of the PCN-250 particles on the polypropylene membrane. Before use, the resulting PCN separator was dried at 80 °C for 12 h in a vacuum oven.

2.5. Lithium–Selenium Cell (Li/Se Cell) Assembly. Cathode materials were prepared by making a slurry of Se@AC, the PTFE binder, and carbon black (Super P) at an 80:10:10 ratio (w/w/w) unless otherwise noted. The Se loading was ~ 1 to 1.5 mg/cm^2 ,^{2,31,37–39} similar to previous studies, to minimize the effect of volume expansion and contraction during charge/discharge that might affect the electrochemical performance. The slurry was coated onto the current collector and dried at 120 °C for 3 h in a vacuum oven to form the working electrode. The CR2032-type coin cells were assembled in an argon-filled glovebox with the moisture and oxygen content below 1 ppm. In all experiments, $\sim 25 \mu\text{L}$ of 1 M LiTFSI in 1:1 dimethoxyethane (DME)/1,3-dioxolane (DOL) (v/v) were used as the electrolyte, unless otherwise noted. In addition, LiNO_3 (1 wt %) was used as an additive to aid in the formation of the solid electrolyte interface at the lithium-metal anode. The anode was prepared by directly pressing lithium metal foils onto a 15.8 mm diameter stainless steel disk. The PCN separator was cut into 18 mm disks and placed in the cells. The conventional polypropylene separator was used as a control.

2.6. Permeation Tests. Permeation tests were conducted in a Li/Se full cell in the H-type cell configuration. The two chambers of the cell were separated by polypropylene or the PCN separator. The Se cathode was prepared using 8 mg of Se@AC, 1 mg of the PTFE binder, and 1 mg of the Super P mixture on a $1 \times 2 \text{ cm}^2$ stainless steel mesh. The selenium loading of the cathode was $\sim 2 \text{ mg}/\text{cm}^2$, slightly higher than that in the CR2032 cells to ensure the visible formation of the polyselenides. The 0.2C (based on theoretical capacity) current rate was applied to discharge the cell at 30 °C. To investigate the formation of soluble polyselenides and their diffusion through the separator, images were captured during 48 h.

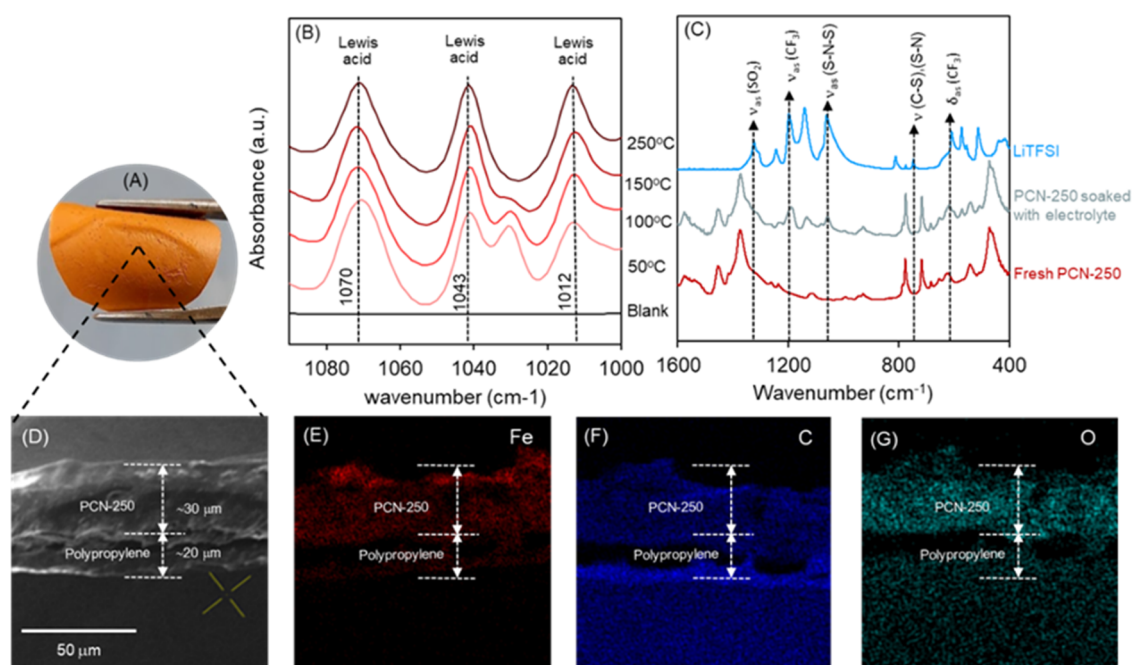


Figure 1. Illustration of a flexible MOF separator (A). DRIFT spectra of PCN-250 with pyridine as a probe molecule (B). FTIR spectra of PCN-250 soaked in electrolytes (C) and SEM micrographs of the cross-sectional area of the MOF separator (D), and its elemental mapping (E–G).

2.7. Open-Circuit Voltage (OCV). The open-circuit voltage of the cell was measured with a BioLogic SP-200 potentiostat/galvanostat using a Li/Se cell. The Li-metal was used as both the reference electrode and the anode. The Se cathode consisted of Se@AC, the PTFE binder, and carbon black (Super P) at an 80:10:10 ratio (w/w/w). The OCV of the cell was recorded at 30 °C for 12 h.

2.8. Cyclic Voltammetry. Cyclic voltammetry (CV) was performed by Autolab using the Li/Se cell. Cyclic voltammetry was conducted between 0.5 and 3.0 V at a scan rate of 0.1 mV/s. Then, the scan rate was varied from 0.1 to 0.2, 0.7, and 1.0 mV/s to determine the lithium-ion diffusion coefficient (D_{Li^+}) by the Randles–Sevcik equation (eq 1).⁴⁰

$$I_p = 2.69 \times 10^5 n^{1.5} A C_{\text{Li}} D_{\text{Li}^+}^{0.5} \nu^{0.5} \quad (1)$$

where I_p is the peak current (Amps), n is the number of electrons transferred in the redox event, C_{Li} denotes the concentration (mol/cm³), A represents the area of the electrode (cm²), and ν represents the scan rate (V/s).

2.9. Li-Ion Transference Number (t_{Li^+}). The Li^+ transference number is defined as a fraction of the overall charge transferred by species containing Li^+ .⁴¹ CR2032-type coin cells using the Li/Li symmetric cell configuration were assembled in an argon-filled glovebox. The cells were left in an open-circuit condition for at least 12 h to equilibrate prior to measurement. The DC polarization method was applied, and the t_{Li^+} was calculated based on the Bruce–Vincent method by eq 2.⁴²

$$t_{\text{Li}^+} = \frac{I_{\text{ss}}(\Delta V - I_0 R_0)}{I_0(\Delta V - I_{\text{ss}} R_{\text{ss}})} \quad (2)$$

where I_0 and I_{ss} represented the initial and steady-state current, respectively. The values of R_0 and R_{ss} were calculated from EIS measurements before and after perturbation at $\Delta V = 10$ mV.

Li^+ transference numbers close to 1 are indicative of low anion motion and are conducive to cell operation without the development of excessive concentration gradients, a condition that increases the efficiency of the cell.⁴³

2.10. Galvanostatic Lithium Cycling Performance. Galvanostatic cycling experiments were conducted using symmetric Li/Li cells with 1 M LiTFSI in a 1:1 DME:DOL (v/v) ratio to evaluate the lithium plating/stripping behaviors using the PCN separator. The

experiments were performed at 30 °C, a 1 mA/cm² current density, and a 30 min plating/stripping interval. Cells with the polypropylene separator were used as a control.

2.11. Electrochemical Performance. Galvanostatic charge/discharge tests were performed at C/10 for 50 cycles and C/5 and 1C for 500 cycles using an Arbin BT2000 battery testing unit (College Station, TX) in a voltage window of 1.0–3.0 V versus Li/Li⁺ to determine the cycling stability of the Li/Se cells. The current rate was calculated based on the weight of selenium (1C = ~675 mA/g theoretical capacity). Before electrochemical testing, the cells were treated with 10 cycles of galvanostatic charge/discharge at a low rate of C/5 for activation. The Coulombic efficiency and capacity retention of the cells after cycling were calculated as follows (eqs 3–5)

$$\text{Coulombic efficiency (CE)} = \frac{\text{charge capacity}}{\text{discharge capacity}} \times 100 \quad (3)$$

$$\text{capacity retention (\%)} = \frac{\text{final capacity}}{\text{initial capacity}} \times 100 \quad (4)$$

$$\begin{aligned} \text{capacity decay rate (\%/cycle)} \\ = \frac{\text{initial capacity} - \text{final capacity}}{\text{initial capacity} \times \text{cycle number}} \times 100 \end{aligned} \quad (5)$$

3. RESULTS

We first fabricated the PCN-250-modified separator and evaluated its ability to prevent self-discharge from the diffusion of polyselenides. Then, we assessed the electrochemical performance and cycle time of lithium–selenium cells with a PCN-250-modified separator (PCN separator).

3.1. Lewis Acid Characteristics of PCN-250 and the Morphology of the PCN Separator. To determine the Lewis acid characteristics of PCN-250, we performed diffuse reflectance infrared Fourier transform spectroscopy (DRIFTS) with adsorbed pyridine at 50–250 °C (Figure 1B). The blank experiments (without pyridine adsorption) did not show any features between 1000 and 1100 cm⁻¹. The peaks at 1012,

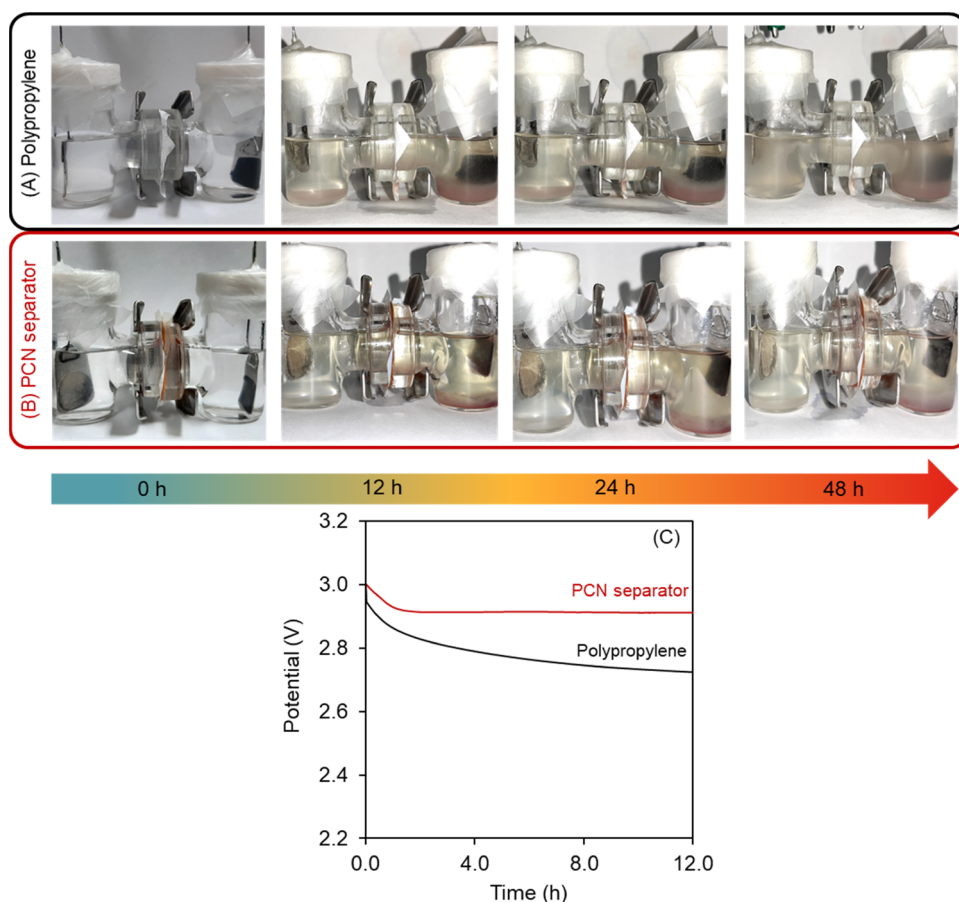


Figure 2. Permeation tests of polypropylene (A) and PCN (B) separators over 48 h in the H-type cells and open-circuit voltage (OCV) retention profiles over 12 h relaxation (C).

1043, and 1070 cm^{-1} indicated the presence of Lewis acid sites. Moreover, the presence of these peaks at an elevated temperature (250 $^{\circ}\text{C}$) suggested a high strength of the Lewis acid sites of PCN-250. To evaluate the Lewis acid–Lewis base interaction between PCN-250 and TFSI $^{-}$, we performed FTIR on the PCN-250 soaked in the solvent (1:1 DME/DOL (v/v)) and electrolyte (1 M LiTFSI in 1:1 DME/DOL (v/v)) (Figure 1C). As a control, the FTIR spectrum of LiTFSI showed unique characteristic peaks of TFSI $^{-}$ at 570, 750, 1051, 1085, 1150, 1192, 1335, and 1364 cm^{-1} (Figure 1C, Table S2).⁴⁴ Next, we soaked PCN-250 materials in the electrolyte for 30 min and washed them with the 1:1 DME/DOL (v/v) solvent to remove physisorbed species. We still observed the peaks of TFSI $^{-}$ at 750, 1051, and 1192 cm^{-1} that suggested a strong interaction between the Lewis acid and Lewis base.

We then used the resulting PCN-250 to fabricate the MOF separator (Figure 1A). The MOF separator was flexible, and the thickness of the MOF layer was $\sim 30\ \mu\text{m}$. Elemental mapping of the PCN separator showed a uniform dispersion of $\text{Fe}_3\text{-}\mu^3\text{-oxo}$ clusters (Figure 1E,G). In addition, the FTIR spectrum of the PCN separator had the characteristics of PCN-250 (Figure S5).

3.2. PCN Separator Prevented Polyselenide Permeation. To assess the interaction between the PCN separator and polyselenides, we performed *in situ* permeation measurements in the H-type cell during 48 h at C/5. The H-type cell consisted of a Li/Se cell with the PCN separator (Figure 2B). As a control, both sides of the cell with the polypropylene separator were clear initially. After discharge, a light brown

color formed on the cathode side (right), indicating the formation of lithium polyselenides. During prolonged discharging, the dissolved polyselenides were concentrated, as shown by the solution's darker color on the cathode side. Moreover, we observed the light brown color on the anode side, which suggested diffusion of the soluble long-chain polyselenides to the anode side. In the case of the PCN separator, although we observed the formation of soluble polyselenides on the cathode side, they did not diffuse to the anode side. Thus, the PCN separator suppressed the diffusion of the soluble polyselenides.

3.3. PCN Separator Prevents Self-Discharge Process.

One of the major challenges in the practical use of Li–Se batteries is their self-discharge caused by the diffusion of polyselenides. To determine the ability of the PCN separator to prevent self-discharging, we evaluated the open-circuit voltage (OCV) behavior of Li/Se cells with the PCN separator during 12 h (Figure 2C). When we used polypropylene as a control, the open-circuit potential continually decreased and reached 2.72 V after 12 h. This continual decrease in the open-circuit voltage occurred because of the diffusion of soluble polyselenides and reaction with the lithium anode. When we used the PCN separator, the open-circuit potential dropped slightly and was maintained at 2.91 V after 2 h. These results suggested the suppression of the diffusion of polyselenides by the PCN separator. These OCV results corroborated the permeation test (Figure 2B).

3.4. PCN Separator as an Anionic Sieve to Enhance the Li $^{+}$ Plating/Stripping Stability. To assess the relative

Li^+ transport in the cell with the PCN separator, we performed Li^+ transference number measurements. As a control, the Li^+ transference number of the cell with the polypropylene separator was 0.38 (Figure 3A), similar to reported values.^{45–47}

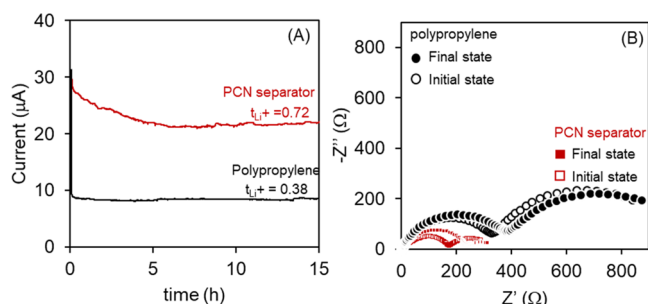


Figure 3. Changes of current with time during polarization of a Li/Li symmetric cell with PCN and polypropylene separators in the fresh electrolyte during 15 h at 30 °C under 10 mV potential (A) and Nyquist plots of the impedance spectra before and after polarization (B).

The cell with the PCN separator yielded a Li^+ transference number of 0.72, much higher than that of the cell with the polypropylene separator. This substantial increase in the Li^+ transference number indicated the facile and selective transit of Li^+ through the PCN separator. Moreover, these results also implied that the PCN separator prevented the diffusion of TFSI anions to the anode side, in contrast to the property of the polypropylene separator. These results further explained the presence of TFSI[−] peaks after soaking PCN-250 in the electrolyte (Figure 1C).

Figure 3B shows the Nyquist plots of the impedance experiment before and after polarization. We fitted the Nyquist plots with the equivalent circuit and obtained the charge transfer resistance (R_2) and Warburg resistance (W_2 , Table S3). The R_2 of the fresh cell (initial) with the polypropylene separator was 332 Ω, which agreed with reported values.^{48,49} The R_2 of the PCN separator was lower than the R_2 with the polypropylene separator, which suggested that the PCN layer improved the electrochemical reaction kinetics.^{49,50} After

polarization, we observed an increase in the R_2 of the cell with both separators, which indicated the decomposition of the Li-metal.^{48,51} Another significant finding from the impedance spectra was the W_2 , which explained the formation of the solid electrolyte interface due to the decomposition of the solvent and TFSI anion on the Li surface.^{48,51,52} For the cell with the PCN separator, the W_2 was much lower than the W_2 with the polypropylene separator (Figure 3B). One reason for this difference was that the PCN separator restricted the diffusion of the TFSI anion to the Li-metal. As a result, the formed solid electrolyte interface layer in the cell with the PCN separator was thinner than that with the polypropylene separator.

To determine whether the PCN separator enhanced lithium cycling stability, we performed galvanostatic cycling experiments using symmetric Li/Li cells containing 1M LiTFSI in a 1:1 DME/DOL (v/v) ratio with the PCN separator. The voltage profile of the lithium metal working electrode (WE) during constant current lithium plating and stripping at 1 mA/cm² for 500 h is presented in Figure 4A. The positive potentials of the lithium WE against the Li/Li⁺ reference electrode (RE) represent the overpotentials that appear during lithium stripping, whereas the negative potentials represent the overpotentials during lithium plating on the WE. The voltage polarization of the cell with a PCN separator was stable over 500 h. As a control, we performed the cycling experiment using the symmetric cell with a polypropylene separator. The voltage polarization of the polypropylene separator cell was stable up to 290 h and then gradually decreased in voltage because of the short circuit.^{53–57} After 290 h, we observed the overpotential (circled, Figure 4C,D) in the polypropylene separator due to the growth of lithium dendrites^{58–61} from the uneven plating behavior of lithium,^{62,63} which penetrated the polypropylene separator.⁶⁴ The short-circuit of the cell with the polypropylene separator further explained the low lithium transference number. This low lithium transference number of the polypropylene separator cell indicated the presence of free anions that hinder the fast lithium-ion diffusion and result in the uneven lithium plating and dendrite growth.^{65,66} The stable Li plating/stripping profiles over 500 h without any short circuit of the cell with the PCN separator suggested uniform lithium plating and corroborated the high lithium-ion trans-

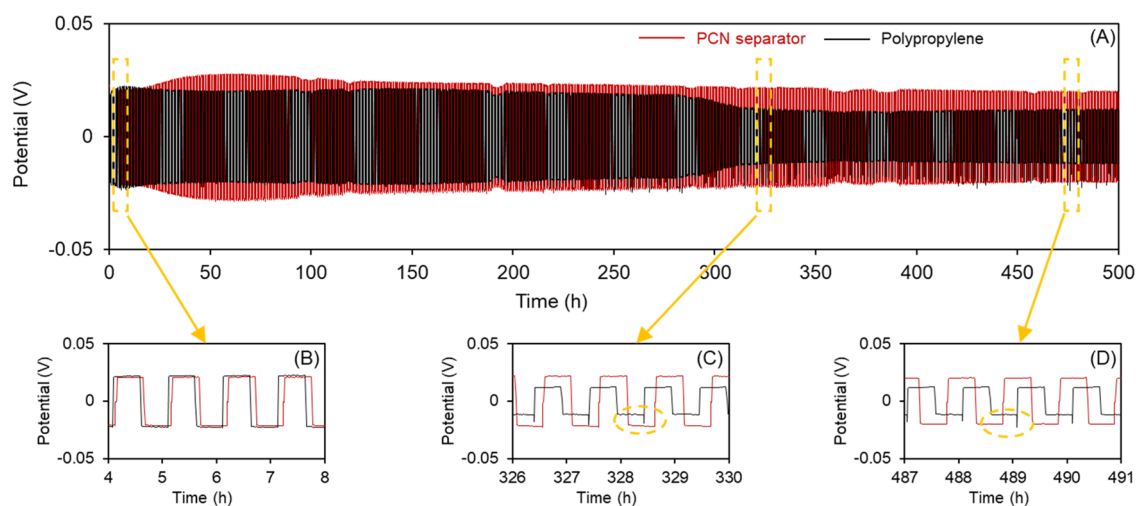


Figure 4. Galvanostatic cycling voltage profiles of a Li/Li symmetric cell cycled at 1 mA/cm² (0.5 mAh/cm²) for 500 h with PCN and polypropylene separators (A), voltage profiles from 4 to 8 h (B), 326 to 330 h (C), and 487 to 491 h (D). Yellow circles indicate overpotentials from the cell with the polypropylene separator.

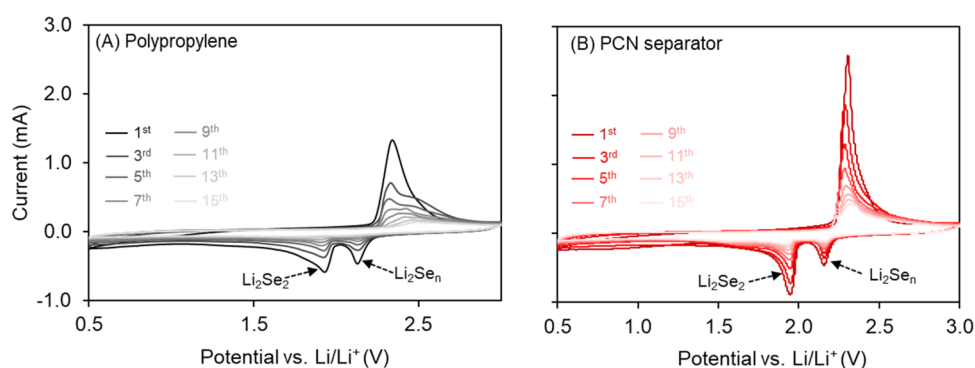


Figure 5. Cyclic voltammetry of cells with polypropylene (A) and PCN (B) separators at a scan rate of 0.1 mV/s at 30 °C.

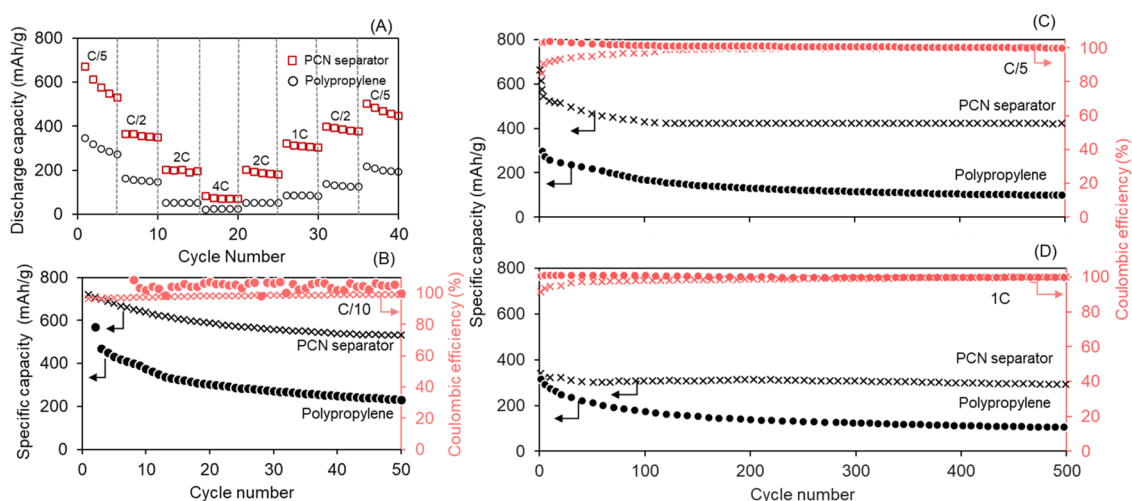


Figure 6. Rate performance with PCN and polypropylene separators at various C-rates from C/5 to 4C (A). Long-term cycling performance of the cells with a PCN separator at a rate of C/10 over 50 cycles (B), C/5 (C), and 1C (D) over 500 cycles at 30 °C.

ference number. These results suggested that the PCN separator was a cation-selective membrane that restricted anion mobility, promoted uniform Li deposition, and suppressed the growth of the dendrite.

3.5. Cyclic Voltammetry. To investigate the redox behavior of selenium in the electrolyte, we performed cyclic voltammetry on the cell with the PCN separator (Figure 5). As a control, the cell with the polypropylene separator showed two reduction peaks (2.2 and 1.9 V) and one oxidation peak (2.4 V). Initially, the cell with the PCN separator exhibited two reduction peaks and one oxidation peak. The two reduction peaks at 1.9 and 2.2 V revealed multiple reduction transformations of selenium into long-chain polyselenides (Li_2Se_x , $4 \leq x \leq 8$) and subsequent reduction of these long-chain lithium polyselenides to short-chain lithium selenides (Li_2Se_2 and Li_2Se) during the discharging (delithiation) process.¹³ Interestingly, cells with both separators showed decreasing peak currents over 15 cycles, which suggested Se cathode dissolution into the electrolyte.^{67,68} We also observed the evolution of a small peak at 1.4 V for five cycles, which we assigned to reduction of LiNO_3 .^{69,70} The one oxidation peak at 2.4 V started to acquire a shoulder after three cycles; this shoulder corresponded to conversion of lithium selenides to polyselenides and eventually solid $\text{Li}_2\text{Se}_2/\text{Li}_2\text{Se}$ ^{71–74} and suggested intensive polarization and poor stability of the polyselenides in the cathode side. Although the cyclic voltammograms of the cell with either separator showed similar cathodic and anodic features, the peaks were broader

for the cell with polypropylene. The cell with the PCN separator showed higher cathodic and anodic peak currents compared with the cell with the polypropylene separator, which suggested that the PCN separator enabled rapid redox kinetics.⁷⁵

Next, we determined the diffusion coefficients using the cyclic voltammograms at different scan rates (Figure S6). The calculated diffusion coefficients for the cell with the polypropylene separator were $\sim 10^{-13}$ to 10^{-12} cm^2/s (Table S4). These values agreed with the reported values.⁷⁶ For the PCN separator, the calculated diffusion coefficients were 10^{-12} – 10^{-11} cm^2/s . A higher diffusion coefficient of the cell with the PCN separator, compared with the polypropylene separator, suggested that the PCN separator had better electrochemical performance⁷⁶ and corroborated the lower charge transfer resistance measured by impedance spectroscopy (Figure 3B).

3.6. Electrochemical Performance of the Cell with a PCN Separator. To better understand the cell redox behavior, we measured the electrochemical performance of Li/Se cells with the PCN separator at different charge/discharge rates (C-rates). The cell with a PCN separator had better performance than the cell with the polypropylene separator (Figure 6A). When cycling at different C-rates, the capacities of the cell with the PCN separator remained relatively constant at 510 mAh/g for C/5, 360 mAh/g for C/2, 190 mAh/g for 2C, and 71 mAh/g for 4C. Then, the capacity returned to 482 mAh/g at C/5.

The Coulombic efficiency is a key indicator of cycling capability in a commercial cell. To evaluate the capacity of the cell, we initially performed galvanostatic charge–discharge of the cell with both separators at a C/10 rate for 50 cycles (Figure 6B). The Li–Se cell with the polypropylene separator lost significant capacity and ended with 228 mAh/g after 50 cycles. Conversely, the cell with the PCN separator maintained a reversible capacity of 522 mAh/g after 50 cycles. These results demonstrated that the PCN separator improved electrochemical performance and capacity retention compared with the polypropylene separator.

Next, we investigated the long-term cycle stability of the cell with the PCN separator. The cells were cycled at C/5 and 1C for 500 cycles (Figure 6C,D). The cell with the PCN separator had a stable reversible capacity from an initial capacity of 661 mAh/g that became relatively stable (423 mAh/g) at C/5 after the 100th cycle. This initial process of ~100 cycles was attributed to activation of the Li–Se cells leading to a highly reversible and stable electrochemical performance, consistent with the observation in Li–S cells.⁷⁷ The capacity retention rate of ~64% with a decay rate as low as 0.07% per cycle for 500 cycles suggested stable kinetics of the cells with the PCN separator. These results demonstrated reversible efficiency and kinetics of the cell using a PCN separator compared with the cell with a polypropylene separator, consistent with the stable electrochemical performance of the CV measurement.

As a control, the cell with the polypropylene separator had lower capacity than the PCN separator cell at both C/5 and 1C. Moreover, the cell with the polypropylene separator required an initial activation as shown in a progressive increase in CE at both C/5 and 1C. When cycled at C/5, the cell with the polypropylene separator demonstrated an initial discharge capacity of 350 mAh/g, followed by a progressive decrease in capacity to 102 mAh/g after 500 cycles. Thus, the capacity retention of the cell with polypropylene was 29% with an average decay rate of 0.14% per cycle for 500 cycles. Next, we cycled the cell at 1C. As expected, the discharge capacity of the cell with the polypropylene separator dropped rapidly to 107 mAh/g after 500 cycles, whereas the discharge capacity of the cell with the PCN separator remained relatively constant at 292 mAh/g with a >98% CE for 500 cycles. We did not observe any change in the morphology of the PCN separator after 500 cycles at 1C (Figure S7).

3.7. Characterization of the Spent PCN Separator. To identify the function of the PCN separator, we performed XPS on the spent PCN separator at C/5 after 50 cycles. The peak deconvolution of the Se 3d region produces two doublet peaks (Figure 7A). The first, strong peak, located at about 54.9 eV, could be attributed to the Se–Se bonds of the backbone structure of chain-like Se_n (2 < n < 8) molecules.^{31,74,78,79} The other, much weaker doublet peak at 57.9 eV, originated from the terminal Se atoms (most likely forming Se–C or Se–O bonds) of such chain-like molecules. The peak deconvolution of the C 1s spectrum yielded four main components at 284.4, 286.3, 288.1, and 290.5 eV, which were identified as the sp²-hybridized carbon (C=C), hydroxyl or epoxy group (C–O), carbonyl group (C=O), and carboxyl group (O–C=O) or C–Se group, respectively (Figure 7B). There were also two weak peaks at 283.3 and 293.3 eV, but the origins of these peaks were unclear. These results suggested that the PCN separator immobilized the polyselenides, corroborating the self-discharging and permeation tests. We postulated that the immobilization of polyselenides occurred by the interaction

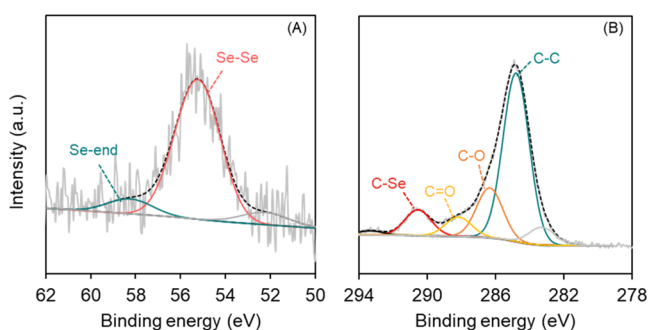


Figure 7. X-ray photoelectron spectra of the Se 3d (A) and C 1s (B) of the spent PCN separator on the cathode side.

between the Lewis base polyselenides and Lewis acid sites of PCN-250, as shown in the DRIFT spectrum of PCN-250.

4. DISCUSSION

We evaluated the efficacy of PCN separators to suppress the polyselenides shuttling between electrodes. The shuttling of polyselenides leads to severe self-discharge, capacity fade, low Coulombic efficiency, and cycling instability. The PCN separator eliminated these issues by blocking the diffusion of polyselenides. This blocking function enhanced Li⁺ transport, long-term cycling stability, and capacity retention as evidenced by a discharge capacity of 423 mAh/g at C/5 and 292 mAh/g with a >98% Coulombic efficiency at 1C over 500 cycles.

One of our most significant findings is that the PCN separator acted as a cation-selective membrane, which simultaneously blocked the shuttling of polyselenides and TFSI anions. Most current work on modified separators for Li–Se cells is aimed at suppressing only the shuttling of polyselenides (Table S5). The immobilization of TFSI anions, a major contributor to the nonuniform Li deposition, has not been investigated widely. Our permeation and cycling tests demonstrated the ability of the PCN separator to suppress the diffusion of polyselenides and promote uniform lithium nucleation and growth, which prolonged the cell life and prevented Li dendrite growth. A possible reason for the PCN separator blocking of polyselenides and promoting stable lithium deposition is that the Lewis acid sites of PCN-250 anchored the Lewis bases, namely, polyselenides²² and TFSI[−].²³ The chemical barriers to polyselenides and TFSI[−] afforded by the PCN separator slowed the loss of active materials (Li and Se) and improved Li⁺ transport (high Li⁺ transference number), enhancing the capacity retention and long-term cycling stability.

The use of modified separators is a key strategy for suppressing the shuttling of polysulfides. MOFs have been used as separator modifiers to prevent the diffusion of the polysulfides for Li–S batteries (Table S6). The combination of a porous structure and uniform Lewis acid sites of MOFs allowed the transport of lithium ions and suppressed shuttling of polysulfides (Lewis base) of Li–S systems. Chen et al.⁸⁰ synthesized a Ni₃(HITP)₂-modified separator for Li–S cells and showed that the cell reached ~585 mAh/g after 300 cycles at C/2. Although they observed that the cell with the Ni₃(HITP)₂-modified separator delivered a better performance at C/2 over 300 cycles, the capacity progressively decayed. Qi et al.⁸¹ used the MIL-125(Ti)-modified separator for Li–S batteries. They found that the MIL-125(Ti) separator retained the capacity and reached 726 mAh/g at C/5 after 200 cycles.

Suriyakumar et al.⁸² applied the Mn–BTC MOF-modified separator in Li–S batteries at C/10 over 80 cycles. They found that the cell with the Mn–MOF separator showed superior capacity retention than that with the polypropylene separator. These prior results suggested that different MOFs interacted differently with polysulfides.

The application of the MOF-modified separator in lithium–selenium batteries has not been assessed. A lack of this knowledge limits our ability to speed the commercialization of Li–Se batteries. Thus, we compared the PCN separator with other reported multilayer modified separators for Li–Se batteries, such as graphene, MXene, and carbon nanotubes (Table S5).^{83,84} The electrochemical performance of the PCN separator was comparable and even superior to other modified separators in terms of capacity retention, long-term stability (500 cycles), Li⁺ transference number, and stability at a high current rate. This information will help design yet more effective separators for Li–Se batteries. We discovered that the PCN separator restricted diffusion of polyselenides and TFSI[−], which prevented the uncontrollable growth of the lithium dendrite and extended cell life.

In theory, the Lewis acid characteristics of PCN-250 can interact with TFSI anions (Lewis base). Although our high Li⁺ transference number (0.72) and stable voltage profile using the Li/Li symmetric cell with the PCN separator implied that the ion-conducting performance in the electrolyte was mainly accomplished by Li⁺, further studies should provide direct evidence of the interaction between TFSI[−] and the PCN separator. Moreover, additional studies should decouple the individual contributions of the MOF pore size and Lewis acid sites to the blockade of polyselenides and TFSI anion diffusion.

5. CONCLUSIONS

Shuttling of polyselenides limits the practical use of lithium–selenium batteries. We fabricated PCN separators that mitigated the shuttle effect of polyselenides. The cells demonstrated a high discharge capacity of 423 mAh/g at a C/5 current rate and 292 mAh/g at 1C with a Coulombic efficiency of >98% after 500 cycles. The PCN separator acted as a chemical sieve to suppress the shuttling of polyselenides and promote uniform Li⁺ transport. As a result, the cells could cycle at C/5 and 1C for 500 cycles with high-capacity retention and Coulombic efficiency. Our findings offer a promising perspective on using PCN-250 as a cation-selective membrane to solve two serious problems in lithium–selenium batteries, the shuttle effect of polyselenides and the uncontrollable growth of lithium dendrite. We expect this PCN separator to be a candidate for high-energy-density lithium–selenium batteries and to be used with other alkali-metal chalcogenide battery systems.

■ ASSOCIATED CONTENT

SI Supporting Information

The Supporting Information is available free of charge at <https://pubs.acs.org/doi/10.1021/acsaem.1c01806>.

Physiochemical properties of polypropylene, PCN-250, and the PCN-coated separator; electrochemical performance of Li/Li and Li/Se cells; SEM analysis of the separator after 500 cycles; and comparison between this work and previously reported studies on Li–Se batteries and MOF-based separators (PDF)

■ AUTHOR INFORMATION

Corresponding Author

Noppadon Sathitsuksanoh – Department of Chemical Engineering, University of Louisville, Louisville, Kentucky 40292, United States; orcid.org/0000-0003-1521-9155; Email: n.sathitsuksanoh@louisville.edu

Authors

Md. Anwar Hossain – Department of Chemical Engineering, University of Louisville, Louisville, Kentucky 40292, United States

Sarttrawut Tulaphol – Sustainable Polymer & Innovative Composite Materials Research Group, Department of Chemistry, Faculty of Science, King Mongkut's University of Technology Thonburi, Bangkok 10140, Thailand; orcid.org/0000-0003-2096-2859

Arjun K. Thapa – Conn Center for Renewable Energy Research, University of Louisville, Louisville, Kentucky 40292, United States

Mohammad Shahinur Rahaman – Department of Chemical Engineering, University of Louisville, Louisville, Kentucky 40292, United States

Jacek B. Jasinski – Conn Center for Renewable Energy Research, University of Louisville, Louisville, Kentucky 40292, United States; orcid.org/0000-0002-1297-6145

Hui Wang – Department of Mechanical Engineering, University of Louisville, Louisville, Kentucky 40292, United States; orcid.org/0000-0003-0936-6781

Mahendra K. Sunkara – Department of Chemical Engineering and Conn Center for Renewable Energy Research, University of Louisville, Louisville, Kentucky 40292, United States; orcid.org/0000-0003-2087-5261

Jaroslav Syzdek – Bio-Logic USA LLC, Knoxville, Tennessee 37923, United States

Osman K. Ozdemir – Framergy Inc, College Station, Texas 77845-6371, United States

Jason M. Ornstein – Framergy Inc, College Station, Texas 77845-6371, United States

Complete contact information is available at: <https://pubs.acs.org/doi/10.1021/acsaem.1c01806>

Notes

The authors declare no competing financial interest.

■ ACKNOWLEDGMENTS

A part of this material is based upon the work supported by the National Science Foundation under the Cooperative Agreement No. 1355438 and the Internal Research Grant, Office of the Executive Vice President for Research, University of Louisville. This work was performed in part at the Conn Center for Renewable Energy Research at the University of Louisville, which belongs to the National Science Foundation NNCI KY Manufacturing and Nano Integration Node, supported by ECCS-1542174. The authors would like to thank Framergy, Inc. (College station, TX, USA) for PCN-250 samples used in this study. The authors would like to thank Dr. Howard Fried and Mr. Jinsol Im for their valuable comments and suggestions on the manuscript.

■ REFERENCES

(1) During discharge these materials act as a cathode. We refer to the positive electrodes as cathodes.

- (2) Desilvestro, J.; Haas, O. Metal oxide cathode materials for electrochemical energy storage: a review. *J. Electrochem. Soc.* **1990**, *137*, 5C.
- (3) Liang, Y.; Zhao, C. Z.; Yuan, H.; Chen, Y.; Zhang, W.; Huang, J. Q.; Yu, D.; Liu, Y.; Titirici, M. M.; Chueh, Y. L.; Yu, H.; Zhang, Q. A review of rechargeable batteries for portable electronic devices. *InfoMat* **2019**, *1*, 6–32.
- (4) Xu, J.; Ma, J.; Fan, Q.; Guo, S.; Dou, S. Recent progress in the design of advanced cathode materials and battery models for high-performance lithium-X (X= O₂, S, Se, Te, I₂, Br₂) batteries. *Adv. Mater.* **2017**, *29*, No. 1606454.
- (5) Yao, Y. X.; Zhang, X. Q.; Li, B. Q.; Yan, C.; Chen, P. Y.; Huang, J. Q.; Zhang, Q. A compact inorganic layer for robust anode protection in lithium-sulfur batteries. *InfoMat* **2020**, *2*, 379–388.
- (6) Wei, Z.; Ren, Y.; Sokolowski, J.; Zhu, X.; Wu, G. Mechanistic understanding of the role separators playing in advanced lithium-sulfur batteries. *InfoMat* **2020**, *2*, 483–508.
- (7) Zhang, Y.; Zhang, P.; Zhang, S.; Wang, Z.; Li, N.; Silva, S. R. P.; Shao, G. A flexible metallic TiC nanofiber/vertical graphene 1D/2D heterostructured as active electrocatalyst for advanced Li–S batteries. *InfoMat* **2021**, *3*, 790–803.
- (8) Luo, C.; Xu, Y.; Zhu, Y.; Liu, Y.; Zheng, S.; Liu, Y.; Langrock, A.; Wang, C. Selenium@ mesoporous carbon composite with superior lithium and sodium storage capacity. *ACS Nano* **2013**, *7*, 8003–8010.
- (9) Peramunage, D.; Licht, S. A solid sulfur cathode for aqueous batteries. *Science* **1993**, *261*, 1029–1032.
- (10) Nelson, J.; Misra, S.; Yang, Y.; Jackson, A.; Liu, Y.; Wang, H.; Dai, H.; Andrews, J. C.; Cui, Y.; Toney, M. F. In operando X-ray diffraction and transmission X-ray microscopy of lithium sulfur batteries. *J. Am. Chem. Soc.* **2012**, *134*, 6337–6343.
- (11) Ji, X.; Lee, K. T.; Nazar, L. F. A highly ordered nanostructured carbon–sulphur cathode for lithium–sulphur batteries. *Nat. Mater.* **2009**, *8*, 500–506.
- (12) Zhang, S. S. Liquid electrolyte lithium/sulfur battery: Fundamental chemistry, problems, and solutions. *J. Power Sources* **2013**, *231*, 153–162.
- (13) Abouimrane, A.; Dambournet, D.; Chapman, K. W.; Chupas, P. J.; Weng, W.; Amine, K. A new class of lithium and sodium rechargeable batteries based on selenium and selenium–sulfur as a positive electrode. *J. Am. Chem. Soc.* **2012**, *134*, 4505–4508.
- (14) Cui, Y.; Abouimrane, A.; Lu, J.; Bolin, T.; Ren, Y.; Weng, W.; Sun, C.; Maroni, V.; Heald, S.; Amine, K. (De) Lithiation mechanism of Li/SeS_x (x= 0–7) batteries determined by in situ synchrotron X-ray diffraction and X-ray absorption spectroscopy. *J. Am. Chem. Soc.* **2013**, *135*, 8047–8056.
- (15) Yang, C. P.; Xin, S.; Yin, Y. X.; Ye, H.; Zhang, J.; Guo, Y. G. An advanced selenium–carbon cathode for rechargeable lithium–selenium batteries. *Angew. Chem., Int. Ed.* **2013**, *52*, 8363–8367.
- (16) Eftekhari, A. The rise of lithium–selenium batteries. *Sustainable Energy Fuels* **2017**, *1*, 14–29.
- (17) Tian, H.; Tian, H.; Wang, S.; Chen, S.; Zhang, F.; Song, L.; Liu, H.; Liu, J.; Wang, G. High-power lithium–selenium batteries enabled by atomic cobalt electrocatalyst in hollow carbon cathode. *Nat. Commun.* **2020**, *11*, No. 5025.
- (18) Fang, C.; Yang, S.; Zhao, X.; Du, P.; Xiong, J. Electrospun montmorillonite modified poly (vinylidene fluoride) nanocomposite separators for lithium-ion batteries. *Mater. Res. Bull.* **2016**, *79*, 1–7.
- (19) Xu, H.; Li, D.; Liu, Y.; Jiang, Y.; Li, F.; Xue, B. Preparation of halloysite/polyvinylidene fluoride composite membrane by phase inversion method for lithium ion battery. *J. Alloys Compd.* **2019**, *790*, 305–315.
- (20) Fan, W.; Zhang, L.; Liu, T. Multifunctional second barrier layers for lithium–sulfur batteries. *Mater. Chem. Front.* **2018**, *2*, 235–252.
- (21) Pan, Y.; Chou, S.; Liu, H. K.; Dou, S. X. Functional membrane separators for next-generation high-energy rechargeable batteries. *Natl. Sci. Rev.* **2017**, *4*, 917–933.
- (22) Zhang, F.; Guo, X.; Xiong, P.; Zhang, J.; Song, J.; Yan, K.; Gao, X.; Liu, H.; Wang, G. Interface Engineering of MXene Composite Separator for High-Performance Li–Se and Na–Se Batteries. *Adv. Energy Mater.* **2020**, *10*, No. 2000446.
- (23) Zhao, C. Z.; Zhang, X. Q.; Cheng, X. B.; Zhang, R.; Xu, R.; Chen, P. Y.; Peng, H. J.; Huang, J. Q.; Zhang, Q. An anion-immobilized composite electrolyte for dendrite-free lithium metal anodes. *Proc. Natl. Acad. Sci. U.S.A.* **2017**, *114*, 11069–11074.
- (24) PCN = porous coordination network.
- (25) Cairns, A. J.; Eckert, J.; Wojtas, L.; Thommes, M.; Wallacher, D.; Georgiev, P. A.; Forster, P. M.; Belmabkhout, Y.; Ollivier, J.; Eddaoudi, M. Gaining Insights on the H₂–Sorber Interactions: Robust soc-MOF Platform as a Case Study. *Chem. Mater.* **2016**, *28*, 7353–7361.
- (26) Kirchon, A.; Li, J.; Xia, F.; Day, G. S.; Becker, B.; Chen, W.; Sue, H. J.; Fang, Y.; Zhou, H. C. Modulation versus Templating: Fine-Tuning of Hierarchically Porous PCN-250 Using Fatty Acids To Engineer Guest Adsorption. *Angew. Chem., Int. Ed.* **2019**, *58*, 12425–12430.
- (27) Chen, Y.; Qiao, Z.; Wu, H.; Lv, D.; Shi, R.; Xia, Q.; Zhou, J.; Li, Z. An ethane-trapping MOF PCN-250 for highly selective adsorption of ethane over ethylene. *Chem. Eng. Sci.* **2018**, *175*, 110–117.
- (28) Kirchon, A.; Day, G. S.; Fang, Y.; Banerjee, S.; Ozdemir, O. K.; Zhou, H. C. Suspension processing of microporous metal-organic frameworks: a scalable route to high-quality adsorbents. *iScience* **2018**, *5*, 30–37.
- (29) Yuan, S.; Sun, X.; Pang, J.; Lollar, C.; Qin, J. S.; Perry, Z.; Joseph, E.; Wang, X.; Fang, Y.; Bosch, M.; et al. PCN-250 under pressure: sequential phase transformation and the implications for MOF densification. *Joule* **2017**, *1*, 806–815.
- (30) Lee, J. T.; Zhao, Y.; Kim, H.; Cho, W.; Yushin, G. Sulfur infiltrated activated carbon cathodes for lithium sulfur cells: the combined effects of pore size distribution and electrolyte molarity. *J. Power Sources* **2014**, *248*, 752–761.
- (31) Li, Z.; Yuan, L.; Yi, Z.; Liu, Y.; Huang, Y. Confined selenium within porous carbon nanospheres as cathode for advanced Li–Se batteries. *Nano Energy* **2014**, *9*, 229–236.
- (32) Hall, J. N.; Bollini, P. Metal–Organic Framework MIL-100 Catalyzed Acetalization of Benzaldehyde with Methanol: Lewis or Brønsted Acid Catalysis? *ACS Catal.* **2020**, *10*, 3750–3763.
- (33) Zheng, X. X.; Fang, Z. P.; Dai, Z. J.; Cai, J. M.; Shen, L. J.; Zhang, Y. F.; Au, C. T.; Jiang, L. L. Iron-Based Metal–Organic Frameworks as Platform for H₂S Selective Conversion: Structure-Dependent Desulfurization Activity. *Inorg. Chem.* **2020**, *59*, 4483–4492.
- (34) Volkringer, C.; Leclerc, H.; Lavalley, J. C.; Loiseau, T.; Ferey, G.; Daturi, M.; Vimont, A. Infrared spectroscopy investigation of the acid sites in the metal–organic framework aluminum trimesate MIL-100 (Al). *J. Phys. Chem. C* **2012**, *116*, 5710–5719.
- (35) Osman, A. I.; Abu-Dahrieh, J. K.; Rooney, D. W.; Halawy, S. A.; Mohamed, M. A.; Abdelkader, A. Effect of precursor on the performance of alumina for the dehydration of methanol to dimethyl ether. *Appl. Catal., B* **2012**, *127*, 307–315.
- (36) Santos, K. M. A.; Albuquerque, E. M.; Innocenti, G.; Borges, L. E. P.; Sievers, C.; Fraga, M. A. The role of Brønsted and water-tolerant Lewis acid sites in the cascade aqueous-phase reaction of triose to lactic acid. *ChemCatChem* **2019**, *11*, 3054–3063.
- (37) Yang, C. P.; Xin, S.; Yin, Y. X.; Ye, H.; Zhang, J.; Guo, Y. G. An advanced selenium–carbon cathode for rechargeable lithium–selenium batteries. *Angew. Chem., Int. Ed.* **2013**, *52*, 8363–8367.
- (38) Han, K.; Liu, Z.; Shen, J.; Lin, Y.; Dai, F.; Ye, H. A free-standing and ultralong-life lithium-selenium battery cathode enabled by 3D mesoporous carbon/graphene hierarchical architecture. *Adv. Funct. Mater.* **2015**, *25*, 455–463.
- (39) Jiang, Y.; Ma, X.; Feng, J.; Xiong, S. Selenium in nitrogen-doped microporous carbon spheres for high-performance lithium–selenium batteries. *J. Mater. Chem. A* **2015**, *3*, 4539–4546.
- (40) Mathew, D. E.; Gopi, S.; Kathiresan, M.; Rani, G. J.; Thomas, S.; Stephan, A. M. A porous organic polymer-coated permselective separator mitigating self-discharge of lithium–sulfur batteries. *Mater. Adv.* **2020**, *1*, 648–657.

- (41) Newman, J.; Balsara, N. P. *Electrochemical Systems*, 4th ed.; John Wiley & Sons: Hoboken, NJ, 2021.
- (42) Bruce, P. G.; Vincent, C. A. Steady state current flow in solid binary electrolyte cells. *J. Electroanal. Chem. Interfacial Electrochem.* **1987**, *225*, 1–17.
- (43) Xu, W.; Wang, J.; Ding, F.; Chen, X.; Nasybulin, E.; Zhang, Y.; Zhang, J. G. Lithium metal anodes for rechargeable batteries. *Energy Environ. Sci.* **2014**, *7*, 513–537.
- (44) Ramesh, S.; Liew, C. W. Dielectric and FTIR studies on blending of [xPMMA–(1–x) PVC] with LiTFSI. *Measurement* **2013**, *46*, 1650–1656.
- (45) Zhao, J.; Wang, L.; He, X.; Wan, C.; Jiang, C. Determination of lithium-ion transference numbers in LiPF₆–PC solutions based on electrochemical polarization and NMR measurements. *J. Electrochem. Soc.* **2008**, *155*, A292.
- (46) Li, C.; Qin, B.; Zhang, Y.; Varzi, A.; Passerini, S.; Wang, J.; Dong, J.; Zeng, D.; Liu, Z.; Cheng, H. Single-Ion Conducting Electrolyte Based on Electrospun Nanofibers for High-Performance Lithium Batteries. *Adv. Energy Mater.* **2019**, *9*, No. 1803422.
- (47) Evans, J.; Vincent, C. A.; Bruce, P. G. Electrochemical measurement of transference numbers in polymer electrolytes. *Polymer* **1987**, *28*, 2324–2328.
- (48) Boz, B.; Ford, H. O.; Salvadori, A.; Schaefer, J. L. Porous Polymer Gel Electrolytes Influence Lithium Transference Number and Cycling in Lithium-Ion Batteries. *J. Electron. Mater.* **2021**, *2*, 154–173.
- (49) Huang, D.; Liang, C.; Chen, L.; Tang, M.; Zheng, Z.; Wang, Z. MOF composite fibrous separators for high-rate lithium-ion batteries. *J. Mater. Sci.* **2021**, *56*, 5868–5877.
- (50) Xu, Q.; Hu, G.; Bi, H.; Xiang, H. A trilayer carbon nanotube/Al₂O₃/polypropylene separator for lithium-sulfur batteries. *Ionics* **2015**, *21*, 981–986.
- (51) Merrill, L. C.; Ford, H. O.; Schaefer, J. L. Application of single-ion conducting gel polymer electrolytes in magnesium batteries. *ACS Appl. Energy Mater.* **2019**, *2*, 6355–6363.
- (52) Dhatarwal, H. S.; Chen, Y.-W.; Kuo, J.-L.; Kashyap, H. K. Mechanistic Insight on the Formation of a Solid Electrolyte Interphase (SEI) by an Acetonitrile-Based Superconcentrated [Li]-[TFSI] Electrolyte near Lithium Metal. *J. Phys. Chem. C* **2020**, *124*, 27495–27502.
- (53) Wu, B.; Lochala, J.; Taverne, T.; Xiao, J. The interplay between solid electrolyte interface (SEI) and dendritic lithium growth. *Nano Energy* **2017**, *40*, 34–41.
- (54) Yue, X.-Y.; Wang, W.-W.; Wang, Q.-C.; Meng, J.-K.; Zhang, Z.-Q.; Wu, X.-J.; Yang, X.-Q.; Zhou, Y.-N. CoO nanofiber decorated nickel foams as lithium dendrite suppressing host skeletons for high energy lithium metal batteries. *Energy Storage Mater.* **2018**, *14*, 335–344.
- (55) Chu, H.; Noh, H.; Kim, Y.-J.; Yuk, S.; Lee, J.-H.; Lee, J.; Kwack, H.; Kim, Y.; Yang, D.-K.; Kim, H.-T. Achieving three-dimensional lithium sulfide growth in lithium-sulfur batteries using high-donor-number anions. *Nat. Commun.* **2019**, *10*, No. 188.
- (56) Fan, X.; Ji, X.; Han, F.; Yue, J.; Chen, J.; Chen, L.; Deng, T.; Jiang, J.; Wang, C. Fluorinated solid electrolyte interphase enables highly reversible solid-state Li metal battery. *Sci. Adv.* **2018**, *4*, No. eaau9245.
- (57) Kim, M.-J.; Yang, K.; Kang, H.-J.; Hwang, H. J.; Won, J. C.; Kim, Y. H.; Jun, Y.-S. Polyimide-Coated Glass Microfiber as Polysulfide Perm-Selective Separator for High-Performance Lithium-Sulphur Batteries. *Nanomaterials* **2019**, *9*, No. 1612.
- (58) Zhao, Q.; Hao, Z.; Tang, J.; Xu, X.; Liu, J.; Jin, Y.; Zhang, Q.; Wang, H. Cation-Selective Separators for Addressing the Lithium–Sulfur Battery Challenges. *ChemSusChem* **2021**, *14*, 792–807.
- (59) Yoon, H.; Howlett, P.; Best, A.; Forsyth, M.; Macfarlane, D. Fast charge/discharge of Li metal batteries using an ionic liquid electrolyte. *J. Electrochem. Soc.* **2013**, *160*, A1629.
- (60) Best, A.; Bhatt, A.; Hollenkamp, A. Ionic liquids with the bis (fluorosulfonyl) imide anion: electrochemical properties and applications in battery technology. *J. Electrochem. Soc.* **2010**, *157*, No. A903.
- (61) Bhatt, A.; Best, A.; Huang, J.; Hollenkamp, A. Application of the N-propyl-N-methyl-pyrrolidinium Bis (fluorosulfonyl) imide RTIL Containing Lithium Bis (fluorosulfonyl) imide in Ionic Liquid Based Lithium Batteries. *J. Electrochem. Soc.* **2009**, *157*, No. A66.
- (62) Lu, D.; Tao, J.; Yan, P.; Henderson, W.; Li, Q.; Shao, Y.; Helm, M.; Borodin, O.; Graff, G.; Polzin, B.; et al. Formation of reversible solid electrolyte interface on graphite surface from concentrated electrolytes. *Nano Lett.* **2017**, *17*, 1602–1609.
- (63) Ma, C.; Feng, Y.; Xing, F.; Zhou, L.; Yang, Y.; Xia, Q.; Zhou, L.; Zhang, L.; Chen, L.; Ivey, D.; et al. A borate decorated anion-immobilized solid polymer electrolyte for dendrite-free, long-life Li metal batteries. *J. Mater. Chem. A* **2019**, *7*, 19970–19976.
- (64) Li, Q.; Zhu, S.; Lu, Y. 3D porous Cu current collector/Li-metal composite anode for stable lithium-metal batteries. *Adv. Funct. Mater.* **2017**, *27*, No. 1606422.
- (65) Zhao, C.-Z.; Zhang, X.-Q.; Cheng, X.-B.; Zhang, R.; Xu, R.; Chen, P.-Y.; Peng, H.-J.; Huang, J.-Q.; Zhang, Q. An anion-immobilized composite electrolyte for dendrite-free lithium metal anodes. *Proc. Natl. Acad. Sci. U.S.A.* **2017**, *114*, 11069–11074.
- (66) Huo, H.; Wu, B.; Zhang, T.; Zheng, X.; Ge, L.; Xu, T.; Guo, X.; Sun, X. Anion-immobilized polymer electrolyte achieved by cationic metal-organic framework filler for dendrite-free solid-state batteries. *Energy Storage Mater.* **2019**, *18*, 59–67.
- (67) Cui, Y.; Abouimrane, A.; Lu, J.; Bolin, T.; Ren, Y.; Weng, W.; Sun, C.; Maroni, V. A.; Heald, S. M.; Amine, K. (De) Lithiation mechanism of Li/SeS_x (x = 0–7) batteries determined by in situ synchrotron X-ray diffraction and X-ray absorption spectroscopy. *J. Am. Chem. Soc.* **2013**, *135*, 8047–8056.
- (68) Abouimrane, A.; Dambournet, D.; Chapman, K. W.; Chupas, P. J.; Weng, W.; Amine, K. A new class of lithium and sodium rechargeable batteries based on selenium and selenium–sulfur as a positive electrode. *J. Am. Chem. Soc.* **2012**, *134*, 4505–4508.
- (69) Zhang, S. S. Role of LiNO₃ in rechargeable lithium/sulfur battery. *Electrochim. Acta* **2012**, *70*, 344–348.
- (70) Zhang, S. S. Effect of discharge cutoff voltage on reversibility of lithium/sulfur batteries with LiNO₃-contained electrolyte. *J. Electrochem. Soc.* **2012**, *159*, No. A920.
- (71) Lv, H.; Chen, R.; Wang, X.; Hu, Y.; Wang, Y.; Chen, T.; Ma, L.; Zhu, G.; Liang, J.; Tie, Z. High-performance Li–Se batteries enabled by selenium storage in bottom-up synthesized nitrogen-doped carbon scaffolds. *ACS Appl. Mater. Interfaces* **2017**, *9*, 25232–25238.
- (72) Jiang, S.; Zhang, Z.; Lai, Y.; Qu, Y.; Wang, X.; Li, J. Selenium encapsulated into 3D interconnected hierarchical porous carbon aerogels for lithium–selenium batteries with high rate performance and cycling stability. *J. Power Sources* **2014**, *267*, 394–404.
- (73) Qu, Y.; Zhang, Z.; Jiang, S.; Wang, X.; Lai, Y.; Liu, Y.; Li, J. Confining selenium in nitrogen-containing hierarchical porous carbon for high-rate rechargeable lithium–selenium batteries. *J. Mater. Chem. A* **2014**, *2*, 12255–12261.
- (74) Han, K.; Liu, Z.; Shen, J.; Lin, Y.; Dai, F.; Ye, H. A free-standing and ultralong-life lithium-selenium battery cathode enabled by 3D mesoporous carbon/graphene hierarchical architecture. *Adv. Funct. Mater.* **2015**, *25*, 455–463.
- (75) Zhao, Y.; Liu, M.; Lv, W.; He, Y. B.; Wang, C.; Yun, Q.; Li, B.; Kang, F.; Yang, Q. H. Dense coating of Li₄Ti₅SO₁₂ and graphene mixture on the separator to produce long cycle life of lithium-sulfur battery. *Nano Energy* **2016**, *30*, 1–8.
- (76) Shiraz, M. H. A.; Zhu, H.; Liu, Y.; Sun, X.; Liu, J. Activation-free synthesis of microporous carbon from polyvinylidene fluoride as host materials for lithium-selenium batteries. *J. Power Sources* **2019**, *438*, No. 227059.
- (77) Bai, S.; Liu, X.; Zhu, K.; Wu, S.; Zhou, H. Metal–organic framework-based separator for lithium–sulfur batteries. *Nat. Energy* **2016**, *1*, No. 16094.
- (78) Li, Z.; Yin, L. MOF-derived, N-doped, hierarchically porous carbon sponges as immobilizers to confine selenium as cathodes for

Li–Se batteries with superior storage capacity and perfect cycling stability. *Nanoscale* **2015**, 7, 9597–9606.

(79) Li, S.; Yang, H.; Xu, R.; Jiang, Y.; Gong, Y.; Gu, L.; Yu, Y. Selenium embedded in MOF-derived N-doped microporous carbon polyhedrons as a high performance cathode for sodium–selenium batteries. *Mater. Chem. Front.* **2018**, 2, 1574–1582.

(80) Chen, H.; Xiao, Y.; Chen, C.; Yang, J.; Gao, C.; Chen, Y.; Wu, J.; Shen, Y.; Zhang, W.; Li, S.; et al. Conductive MOF-modified separator for mitigating the shuttle effect of lithium–sulfur battery through a filtration method. *ACS Appl. Mater. Interfaces* **2019**, 11, 11459–11465.

(81) Qi, C.; Xu, L.; Wang, J.; Li, H.; Zhao, C.; Wang, L.; Liu, T. Titanium-containing metal–organic framework modified separator for advanced lithium–sulfur batteries. *ACS Sustainable Chem. Eng.* **2020**, 8, 12968–12975.

(82) Suriyakumar, S.; Kanagaraj, M.; Kathiresan, M.; Angulakshmi, N.; Thomas, S.; Stephan, A. M. Metal-organic frameworks based membrane as a permselective separator for lithium-sulfur batteries. *Electrochim. Acta* **2018**, 265, 151–159.

(83) Fang, R.; Zhou, G.; Pei, S.; Li, F.; Cheng, H. M. Localized polyselenides in a graphene-coated polymer separator for high rate and ultralong life lithium–selenium batteries. *Chem. Commun.* **2015**, 51, 3667–3670.

(84) Zhang, F.; Guo, X.; Xiong, P.; Zhang, J.; Song, J.; Yan, K.; Gao, X.; Liu, H.; Wang, G. Interface Engineering of MXene Composite Separator for High-Performance Li–Se and Na–Se Batteries. *Adv. Energy Mater.* **2020**, 10, No. 2000446.